ACS APPLIED MATERIALS & INTERFACES

Research Article

Cite This: ACS Appl. Mater. Interfaces XXXX, XXX, XXX−XXX

www.acsami.org

Coordination Polymers for High-Capacity Li-Ion Batteries: Metal-Dependent Solid-State Reversibility

Hyun Ho Lee,[†] Jae Bin Lee,[†] Yuwon Park,[‡] Kern Ho Park,[†,‡] Mahmut Sait Okyay,[§] Dong-Seon Shin,[†] Sunghwan Kim,[†] Jongnam Park,[†] Noejung Park,[§] Byeong-Kwan An,[∥] Yoon Seok Jung,[†] Hyun-Wook Lee,*[,†] Kyu Tae Lee,*[,‡] and Sung You Hong*[,†]

[†]School of Energy and Chemical Engineering and [§]Department of Physics, Ulsan National Institute of Science and Technology (UNIST), 50 UNIST-gil, Ulsan 44919, Republic of Korea

[‡]School of Chemical and Biological Engineering, Institute of Chemical Processes, Seoul National University, 599 Gwanangno, Gwanak-gu, Seoul 151-744, Republic of Korea

[∥]Department of Chemistry, The Catholic University of Korea, Bucheon-si, Geyonggi-do 420-753, Republic of Korea

Supporting Information

ABSTRACT: Electrode materials exploiting multielectron-transfer processes are essential components for large-scale energy storage systems. Organic-based electrode materials undergoing distinct molecular redox transformations can intrinsically circumvent the structural instability issue of conventional inorganic-based host materials associated with lattice volume expansion and pulverization. Yet, the fundamental mechanistic understanding of metal−organic coordination polymers toward the reversible electrochemical processes is still lacking. Herein, we demonstrate that metal-dependent spatial proximity and binding affinity play a critical role in the reversible redox processes, as verified by combined ^{13}C solid-state NMR, X-ray absorption spectroscopy, and transmission electron microscopy. During the electrochemical lithiation, in situ generated metallic nanoparticles dispersed in the organic matrix generate electrically conductive paths, synergistically aiding subsequent multielectron transfer to π-conjugated ligands. Comprehensive screening on 3d-metal−organic coordination polymers leads to a high-capacity electrode material, cobalt-2,5-thiophenedicarboxylate, which delivers a stable specific capacity of ∼1100 mA h g^{-1} after 100 cycles.

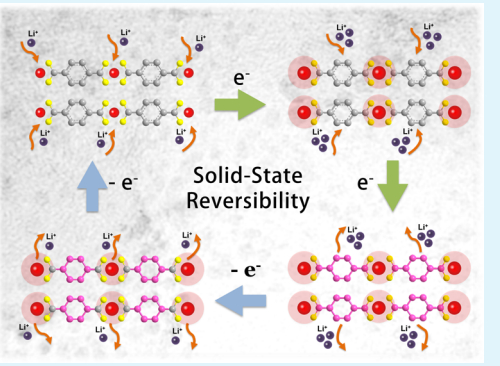

KEYWORDS: *conversion, high capacity, lithium-ion batteries, organic ligand, reaction mechanism*

1. INTRODUCTION

The reversible topotactic transition of two-dimensional inorganic compounds through the intercalation chemistry is the most extensively investigated redox process.[1] However, the limited storage capacity cannot meet the emerging demands of the future society. Alloying process that enlists groups 14 or 15 elements (e.g., Si, Ge, Sn, and P) provides greater capacities by accommodating multiple Li.[2,3] However, it often accompanies low electronic conductivity, slow kinetics, large lattice strains, repeated solid electrolyte interphase (SEI) exposure, pulverization, and capacity loss. In particular, the Park group introduced a high-capacity anode material, SnTe, for sodium-ion or lithium-ion batteries. This tin-based compound experiences unique multistage phase changes associated with topotactic transition, conversion, and alloying pathways.[4] Conventional conversion materials, mostly based on inorganic materials, undergo structural reorganization while forming metallic nanoparticles embedded in a lithiated matrix (Figure 1a).[5−9]

Redox-active organic, organometallic, and coordination compounds have been widely applied as electrode materials thanks to their diverse synthetic strategies, wet-chemical processes, and readily tunable electrochemical properties.[10−15] However, dissolution of small organic molecules in electrolyte solutions leads to severe capacity loss upon cycling. Several synthetic approaches have been reported, including noncovalent immobilization,[16,17] polymerization,[18,19] and macrocyclization.[20,21] The Tarascon group provided one avenue by exploring inverse-Würster-type molecules (Figure 1b). This approach intrinsically circumvents the dissolution penalty by adopting salt structures.[22] In addition, several research groups have reported that binary metal−organic complexes can be applied as high-capacity electrode materials for lithium-ion or sodium-ion batteries, by co-utilizing transition-metal redox couples and redox-active organic ligands.[12,23−32] However, the role of nanosized metallic clusters embedded in an organic ligand matrix toward reversible electrochemical (de)lithiation has remained unclear to date. Herein, we unravel the metal-dependent solid-state redox reversibility of coordination

Received: March 22, 2018
Accepted: June 14, 2018
Published: June 14, 2018

DOI: 10.1021/acsami.8b04678
ACS Appl. Mater. Interfaces XXXX, XXX, XXX−XXX

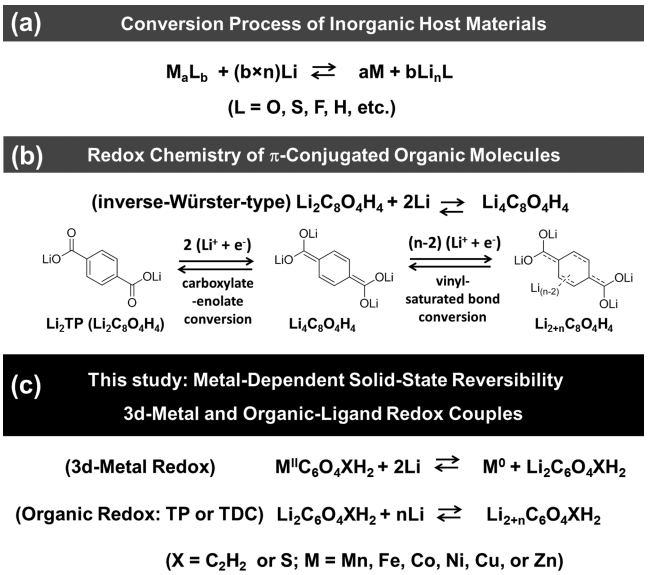

Figure 1. (a) Conventional conversion reaction of inorganic host materials. (b) Redox chemistry of inverse-Würster-type molecules. (c) This study: metal-dependent redox reactions of metal−organic complexes.

polymer frameworks through the comprehensive screening of the first-row transition-metal (3d-metal) cations and inverse-Würster-type molecules. This approach leads to a tailored coordination polymer, cobalt-2,5-thiophenedicarboxylate, which maintains an enhanced reversible capacity of ∼1100 mA h g^{-1} at a high current density of 500 mA g^{-1}.

2. EXPERIMENTAL SECTION

2.1. Sample Preparation and Characterization. Mn, Fe, Co, Ni, Cu, or Zn cation was coordinated with a terephthalate (**TP**) ligand in an aqueous solution via salt metathesis reaction (see the Supporting Information, section I). The crystal structure, number of hydrates, and the thermal stability were estimated by powder X-ray diffraction (XRD) and thermogravimetric/differential thermal analyses (TGA/DSC) (Figures S1 and S2, Supporting Information). Fourier transform infrared (FT-IR) spectra (Figure S3) revealed characteristic asymmetric and symmetric carboxylate vibration peaks, ν_{as} (1569−1535 cm^{-1}) and ν_s (1386−1359 cm^{-1}). Samples were vacuum-annealed to remove crystal water at 150 °C before electrochemical investigations.

2.2. Electrochemical Tests. The activated material was mixed with carbon black (Super P) and binder in a 4:3:1 weight ratio. The electrochemical performance was evaluated using 2032 coin cells with a lithium metal anode and 0.8 M $LiPF_6$ in ethylene carbonate/diethyl carbonate (1:1, v/v) electrolyte solution. Galvanostatic experiments were performed at 25 °C, and specific current densities of 100 or 500 mA g^{-1} were applied to electrode materials.

3. RESULTS AND DISCUSSION

3.1. Electrochemical Properties of Conversion Materials. Coordination polymer architectures comprising divalent 3d-metal cations and **TP** ligand have been chosen because of the well-established synthetic protocols, cost effectiveness, and low environmental impact (see the Supporting Information, sections I & II). Figure 2 shows the potential profiles of anhydrous 3d-metal **TP** samples at a current density of 100 mA g^{-1}. It is noteworthy that redox couples are located not only on the transition metal but also on the inverse-Würster-type **TP** ligand, as depicted in Figure 1c. The potential profiles exhibited a multistage electrochemical lithiation behavior: (i) an abrupt potential drop at 1.0−1.4 V linked to the metal redox couple,[12,23,24,33−35] (ii) a voltage plateau near 0.6−0.8 V attributed to the carboxylate-to-enolate conversion,[12,22,36−38] and (iii) a subsequent sloping profile associated with the progressive vinyl-to-saturated bond conversion[39−41] of the organic scaffold (see Figure 1b). The formation of SEI films or electrically isolated islands brings irreversible capacity loss,[42] resulting in the low initial Coulombic efficiencies (CEs) (78.8% for **CoTP**, 77.0% for **NiTP**, 62.5% for **FeTP**, 50.4% for **CuTP**, 46.9% for **MnTP**, and 32.5% for **ZnTP**). However, the CE values reach close to 100% within a few cycles. Further cycling displays different profiles as compared to the first cycle, typically observed features for the conversion processes undergoing large structural rearrangement.[7,8]

CoTP, **FeTP**, and **NiTP** delivered high reversible charge capacities of 1155, 1143, and 1092 mA h g^{-1} after 10 cycles, respectively, whereas **MnTP**, **CuTP**, and **ZnTP** carried relatively low specific capacities of 794, 604, and 511 mA h g^{-1}, respectively. Most samples showed stable cycle performance (Figure 3a,b). Noticeably, lithiation-induced activation behavior occurred for **MnTP** with gradual capacity drop. The rate performance (Figure 3c) was further investigated, and the discharge capacities of the active materials were recorded by subtracting the Super P contribution (Figure S5). **MnTP** also displayed the poorest rate capability, with a 26% retained capacity with increasing current density from 100 to 2000 mA g^{-1}. **FeTP**, **CoTP**, and **NiTP** exhibited good capacity retention ratios above 63%. Despite diminished capacities, **CuTP** and

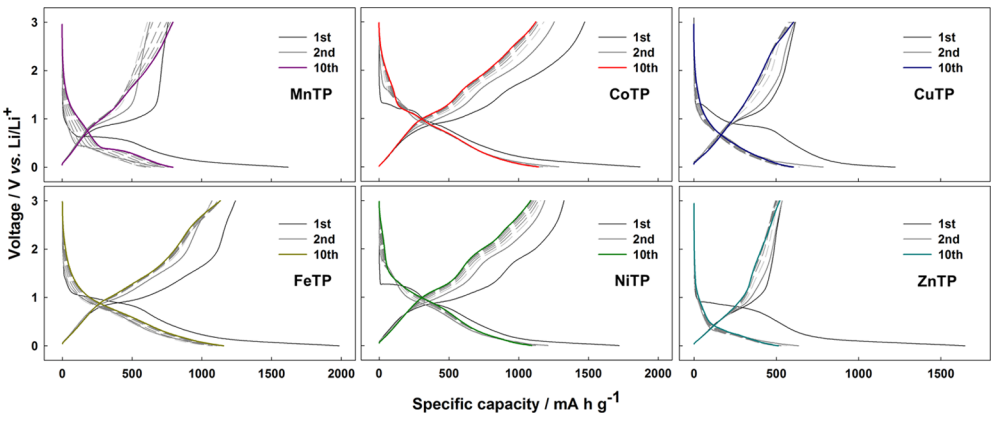

Figure 2. Voltage profiles of 3d-metal **TP**s at a current rate of 100 mA g^{-1}.

DOI: 10.1021/acsami.8b04678
ACS Appl. Mater. Interfaces XXXX, XXX, XXX−XXX

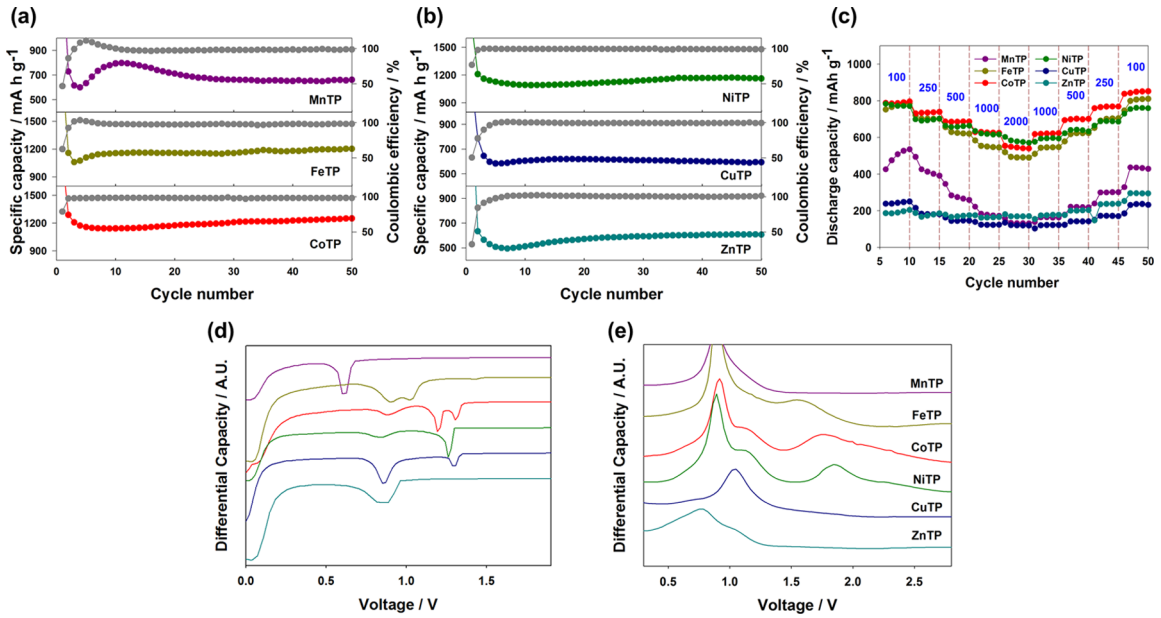

Figure 3. Electrochemical performance of 3d-metal **TPs**: (a,b) cyclability at a current rate of 100 mA g^{-1}. (c) Rate capability (the unit: mA g^{-1}). (d) Electrochemical dQ/dV plot: the first discharge at a current rate of 100 mA g^{-1}. (e) Electrochemical dQ/dV plot: the first recharge at a current rate of 100 mA g^{-1}.

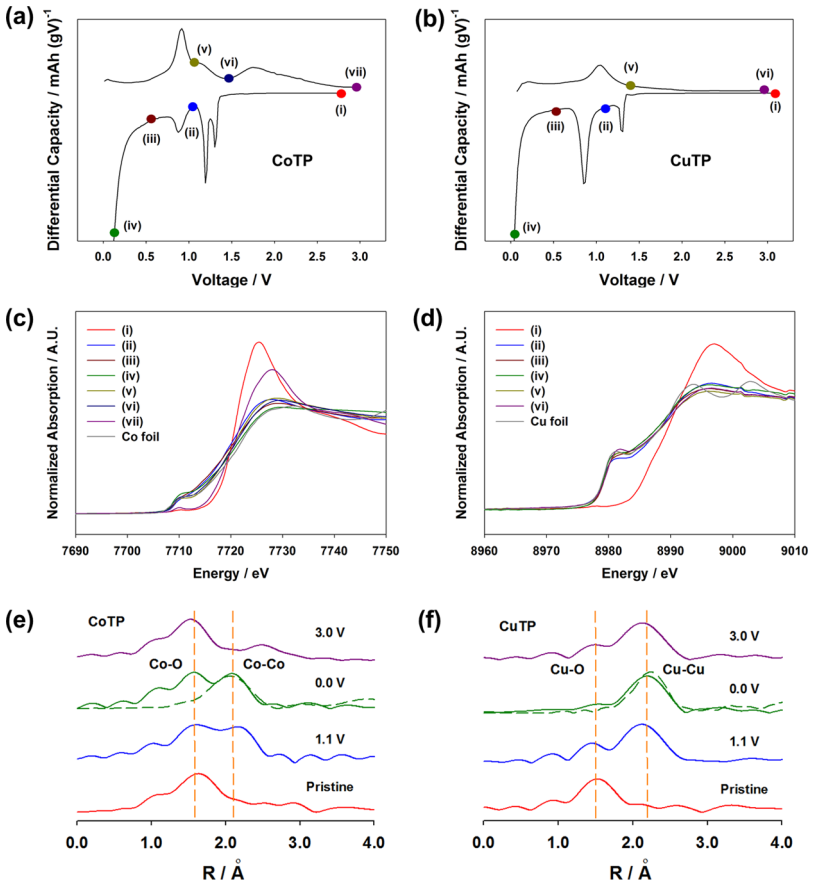

Figure 4. Synchrotron-sourced X-ray absorption spectroscopy (XAS) analyses of **CoTP** and **CuTP**. (a,b) dQ/dV plots for the first cycle. (c,d) Co K-edge and Cu K-edge XANES patterns. (e,f) Co K-edge and Cu K-edge extended X-ray absorption fine structure (EXAFS) patterns. Dashed line represents a metallic standard from Co or Cu foil.

ZnTP showed good rate performance in the range of 1000–2000 mA g^{-1}.

To clarify the electrochemical behaviors, differential capacity (dQ/dV) measurements were also carried out. During the first lithiation step (Figures 3d and S6), **FeTP**, **CoTP**, **NiTP**, and

DOI: 10.1021/acsami.8b04678
ACS Appl. Mater. Interfaces XXXX, XXX, XXX−XXX

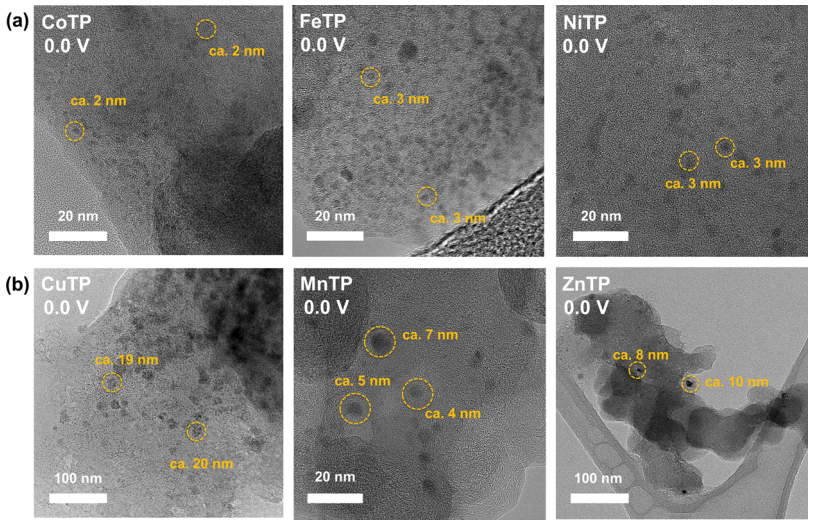

Figure 5. (a) HRTEM images of **CoTP**, **FeTP**, and **NiTP** at 0.0 V. (b) HRTEM images of **CuTP**, **MnTP**, and **ZnTP** at 0.0 V.

CuTP revealed characteristic M(II) reduction peaks at 1.02, 1.19, 1.26, and 1.30 V, respectively. Within the measured voltage range, reductive peaks for **MnTP** and **ZnTP** were not observed, presumably because of their shift to the lower potential region. Subsequent reductive peaks (0.8−0.9 V) are originated from the carboxylate-to-enolate transformation.[22] During the delithiation process (Figure 3e), enolate-to-carboxylate reconversion was observed in a range of 0.74−1.04 V. The regeneration of M(II) cations for **FeTP**, **CoTP**, and **NiTP** was found in the range of 1.55−1.84 V. On the basis of the dQ/dV analysis, the polarization gap (40−260 mV) was much smaller than that of the M(II)/M(0) redox couple (540−580 mV), indicating favorable redox kinetics of the carboxylate-enolate conversion. It is noteworthy that additional capacity is observed in the range of ∼1.5−3.0 V beyond the theoretical capacity estimated from the M(II)/M(0) redox couple, implying the concurrent involvement of the aromaticity recovery process (see also Figure 2). This asymmetrical redox route upon discharge/charge cycling is linked with voltage hysteresis, the characteristic feature for the conversion-type processes.[43,44] However, metal oxidative peaks for **MnTP**, **CuTP**, and **ZnTP** could not be detected. To elucidate the origin of the metal-dependent reversible conversion process, high-capacity/reversible **CoTP** and low-capacity/irreversible **CuTP** were selected as representative models for comparison (Table S1, Supporting Information).

3.2. CoTP Versus CuTP: Spatial Proximity. Synchrotron-sourced ex situ X-ray absorption near-edge structure (XANES) analysis was applied to trace the valence state changes of **CoTP** and **CuTP** on the basis of the redox peaks from the dQ/dV plots (Figure 4a−d). The initial divalent state of **CoTP** was determined from a weak pre-edge peak at 7710 eV, assigned to the 1s → 3d transition. This peak arises from either noncentrosymmetric metal site or 4p−3d orbital mixing.[45] During the first discharge cycle, reduction to metallic cobalt was undoubtedly evidenced by Co K-edge XANES, where the cobalt foil was used as a standard.[46,47] In the reconversion process approaching 3.0 V, regenerated cobalt(II) oxidation states was observed with slight changes in absorption-edge and pre-edge peaks, implying disordered local environment.[47] In sharp contrast, **CuTP** displayed irreversible behavior under the same electrochemical conditions.

Next, ex situ EXAFS study was conducted to unravel their local coordination environments (Figure 4e). The radial distance is given by radial distribution function, which is uncorrected for phase shifts.[48−50] **CoTP** initially displayed a strong Co−O bond. When the redox potential reached 1.1 V, a strong intermetallic Co−Co bond appeared together with the Co−O bond. This indicates that metallic Co is still in close proximity to the oxygen atom from carboxylates (i.e., homogeneously embedded Co particles in organic ligand domains). No pronounced variations were observed until the potential reached 0.0 V. Upon full delithiation up to 3.0 V (reconversion step), the Co−Co metallic bond completely disappeared and a similar spectrum resembling the pristine stage was recovered. In contrast, the EXAFS pattern of **CuTP** upon cycling was distinctly different, as shown in Figure 4f. The intensity of the Cu−O bond became weaker, whereas a strong Cu−Cu correlation appeared after passing through the first reductive peak. At 0.0 V, the intensity of the Cu−O correlation weakened, suggesting that metallic copper clusters were segregated from the organic ligand matrix.[51] During delithiation up to 3.0 V, the spectrum was found to be largely irreversible, where the Cu−Cu bond was mostly intact together with partial recovery of the Cu−O peak. These EXAFS data unequivocally indicate that the spatial arrangement of metallic clusters and organic ligand plays an essential role in determining the molecular structural reorganization and recovery.

To provide information on the spatial distribution of metallic clusters, high-resolution transmission electron microscopy (HRTEM) analyses (Figures 5 and S8) were conducted for both **CoTP** and **CuTP**. After full lithiation to 0.0 V, the average size of the metallic cobalt clusters (yellow circles) is about 2 nm. These nanoparticles are well dispersed in the organic matrix. In contrast, fully reduced metallic copper clusters show segregated structures (yellow circles, ∼20 nm in size). This compositional inhomogeneity can disconnect segregated particles from the organic ligand matrix. To evaluate the role of metal redox process decoupled from organic redox chemistry, a parallel comparison between **CoTP** and **CuTP** was conducted within the potential range of 3.0−1.0 V (Figure S7). Although overall capacity dramatically diminished, the cobalt complex showed better reversibility than the copper complex. Additionally, the metal-dependent binding energies were evaluated by applying

DOI: 10.1021/acsami.8b04678
ACS Appl. Mater. Interfaces XXXX, XXX, XXX−XXX

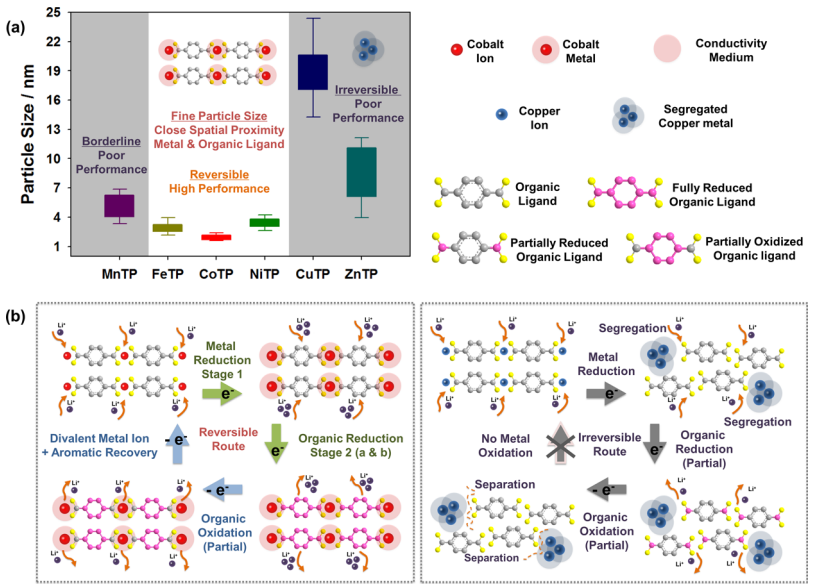

Figure 6. (a) Metallic cluster sizes and solid-state electrochemistry. (b) Schematic illustration of solid-state electrochemical pathways: cobalt- vs copper-molecular complexes.

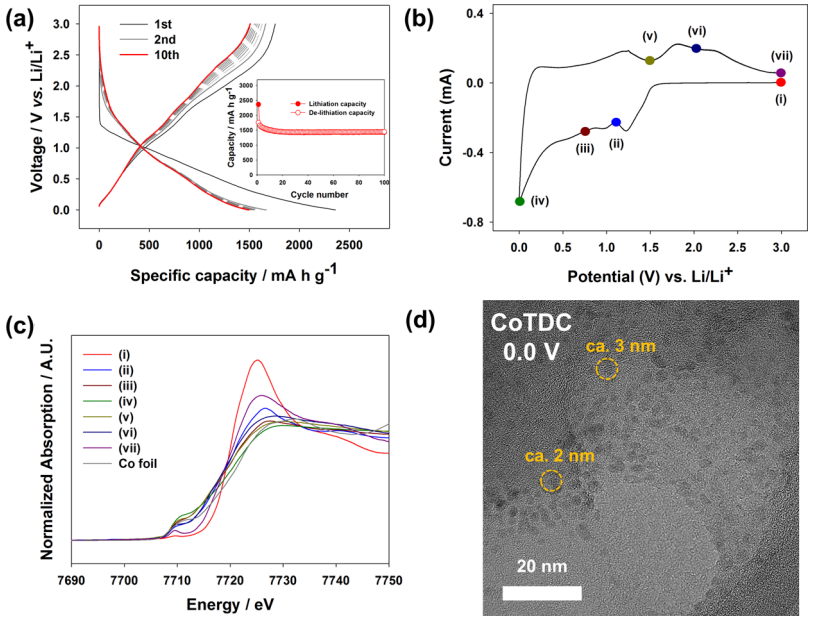

Figure 7. Electrochemical performance, XANES analysis, and HRTEM image of anhydrous **CoTDC**. (a) Voltage profile and cyclability at a current density of 500 mA g^{-1} (inset: cyclability). (b) Cyclic voltammogram of anhydrous **CoTDC**. (c) Co K-edge XANES pattern during the first cycle. (d) HRTEM image at 0.0 V.

the density functional theory (DFT) model system on the basis of metal cluster(s) and single **TP** ligand (for the details, see the Supporting Information, section I-3). It is noteworthy that cobalt clusters strongly coordinate with **TP** ligand, while stabilizing the overall surface energy. In contrast, copper clusters show less effective binding with the ligand, which can result in their segregation of the clusters from the organic matrix and solid-state irreversibility.

3.3. Classification of 3d-Metal TP Complex Systems.

After the initial observations on **CoTP** and **CuTP**, the remaining metal−organic complexes (**MnTP**, **FeTP**, **NiTP**, and **ZnTP**) were further explored. HRTEM images (Figures 5a and S10 in the Supporting Information) of **CoTP**, **FeTP**, and **NiTP** at 0.0 V typically show fine particles mostly below ca. 3 nm. On the other hand, **CuTP**, **MnTP**, and **ZnTP** samples at 0.0 V generally exhibit bigger particle sizes and larger size distributions (Figures 5b and S11). To unravel the valence state changes of 3d-metals, XANES analyses were then performed on a series of 3d-metal **TP** complexes. During the first discharge cycle (Figure S12), **FeTP** and **NiTP** were fully reduced to metallic iron and nickel. In the reconversion process approaching to 3.0 V, they were reconverted into divalent phase with slight variation, sharing the solid-state reversibility features with **CoTP**.

Next, the valence states of **MnTP** were evaluated upon cycling. As shown in Figure S12b, Mn(II)/Mn(0) redox chemistry by the XANES analysis revealed mixed valence state and borderline features. Remarkably, **ZnTP** exhibited unique redox mechanism during electrochemical reaction; when fully

DOI: 10.1021/acsami.8b04678
ACS Appl. Mater. Interfaces XXXX, XXX, XXX−XXX

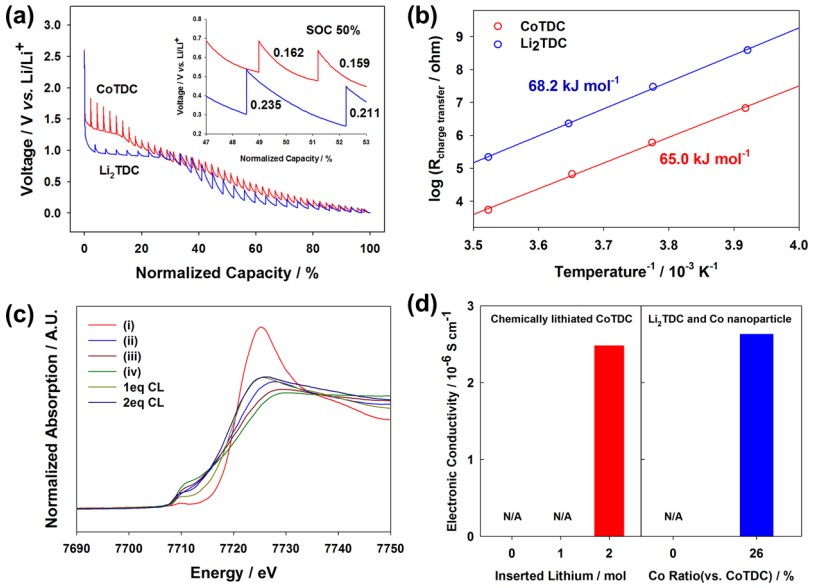

Figure 8. Parallel comparison between **CoTDC** and **Li_2TDC**. (a) Quasi-open-circuit-voltage (QOCV) profiles of anhydrous **CoTDC** and **Li_2TDC** obtained via GITT (inset: QOCV profiles at 50% of SOC). (b) Arrhenius plot of charge-transfer resistance obtained via a symmetric cell at 50% of SOC. (c) Co K-edge XANES spectra of anhydrous **CoTDC** electrode during the first cycle and chemically lithiated anhydrous **CoTDC**. (d) Electronic conductivity measurement: chemical-lithiation (left) and physical mixture (right).

lithiated to 0.0 V, reduction of divalent zinc cation did not stop at the metallic phase but progressively continued to form lithium−zinc (LiZn) alloy (Figure S12b).[52,53] The LiZn phase was further confirmed by HRTEM and the corresponding fast Fourier transform pattern analysis (Figure S11). During the delithiation step approaching to 3.0 V, the white line was not shifted to the pristine stage exhibiting the solid-state irreversibility.

Overall, the 3d-metal **TP** complex systems are categorized into three groups according to the metal-specific electrochemical properties (Figure 6a): type I (**CoTP**, **FeTP**, and **NiTP**)—reversible/high performance group; type II (**MnTP**)—borderline group; and type III (**CuTP** and **ZnTP**)—irreversible/poor performance group. During the lithiation, type I compounds in situ generate metallic cobalt, iron, and nickel clusters in close proximity to the oxygen atom of the carboxylate group. The nanoparticles synergistically can assist successive lithiation to π-conjugated ligands. In contrast, type III compounds display the compositional inhomogeneity (i.e., disconnected metallic or alloy clusters from the organic ligand matrix). It results in an interfacial penalty hampering the multistage molecular rearrangement during the conversion/reconversion reaction (see the schematic illustration in Figure 6b).

3.4. Cobalt^{II}-2,5-thiophenedicarboxylate. Having identified the 3d-metal-dependent solid-state reversibility of type I compounds, our attention was shifted to expand the repertoire of metal−organic coordination polymers. After the comprehensive screening of 3d-metal cations (Supporting Information, section I) and π-conjugated heterocyclic ligands (Supporting Information, section II), cobalt(II) and 2,5-thiophenedicarboxylate (**TDC**) moieties were assembled to yield **CoTDC**·1.5 H_2O via a facile hydrothermal reaction[54,55] (for the details, see the Supporting Information, section III). Powder XRD patterns confirmed the formation of the desired product (Figure S18c). TGA/DSC data revealed the dehydration at ∼240 °C with ∼10 wt % loss, in good agreement with the corresponding number of hydrates (1.5 H_2O) (Figure S18d). The as-prepared sample was further investigated by FT-IR spectroscopy, and the characteristic dicarboxylate peaks were observed at 1515 and 1326 cm^{-1} assigned to ν_{as}(COOCo) and ν_s(COOCo), respectively (Figure S18e). The sample was annealed at 240 °C in vacuo, and the complete removal of the hydrates was confirmed by TGA/DSC and FT-IR spectrum (see Figure S19). Galvanostatic cycling tests were carried out using the annealed and amorphized **CoTDC** (Figures 7a and S20), displaying substantially improved electrochemical performances than aforementioned 3d-metal **TP**s. The reversible specific capacity of **CoTDC** maintained at 1420 mA h g^{-1} after 100 cycles under the current density of 500 mA g^{-1}. After the removal of Super P contribution, the reversible capacity of anhydrous **CoTDC** was estimated to be 1192 mA h g^{-1} corresponding to ∼10 Li per cobalt metal (Figures S21 and S22).

Fully reduced state of **CoTDC** was then examined via ex situ XAS. The valence change was traced with normalized Co K-edge XANES spectra at various points (Figure 7b,c). After passing the first reductive peak at 1.25 V, the pre-edge peak gradually evolved and the white-line intensity concurrently decreased. The **Co(0)/Li_{4+x}TDC** phase (see also eqs 1−2a) during the charge step subsequently recovered divalent features of **CoTDC** (see also EXAFS patterns in Figure S23). HRTEM presents fully reduced nanoparticles in the size range of ∼2−3 nm that are well dispersed in the organic matrix (Figures 7d and S24). Next, ^{13}C-isotope-labeled **CoTDC** (**CoTDC-$^{13}C_1$**) was prepared to enhance the signal sensitivity of ^{13}C NMR spectra (Scheme S2 and Figure S25, Supporting Information). The carboxylate ^{13}C peak was observed in the chemical shift of 170−180 ppm (Figure S26). A broad peak ∼100 ppm region is attributed to Super P. After lithiation and subsequent delithiation, the solid-state ^{13}C NMR spectrum of **CoTDC-$^{13}C_1$** at 3.0 V provided a broad band centered at ∼180 ppm, ascribed to the regenerated carboxylate ^{13}C (Figure S26).

Stage 1: M(II)/M(0) redox couple.

DOI: 10.1021/acsami.8b04678
ACS Appl. Mater. Interfaces XXXX, XXX, XXX−XXX

$$\mathbf{CoTDC}(CoC_6H_2O_4S) + 2Li \rightleftarrows \mathbf{Co}(0) + \mathbf{Li_2TDC}(Li_2C_6H_2O_4S) \quad (1)$$

Stage 2: **TDC** ligand redox couple.
2a. Carboxylate-to-enolate conversion.

$$\mathbf{Li_2TDC}(Li_2C_6H_2O_4S) + 2Li \rightleftarrows \mathbf{Li_4TDC}(Li_4C_6H_2O_4S) \quad (2a)$$

2b. Vinyl-to-saturated bond conversion.

$$\mathbf{Li_4TDC}(Li_4C_6H_2O_4S) + xLi \rightleftarrows \mathbf{Li_{4+x}TDC}(Li_{4+x}C_6H_2O_4S) \quad (2b)$$

3.5. Role of Nanoparticles. Pristine $\mathbf{Li_2TDC}$ in the absence of cobalt nanoparticles exhibited larger polarization, poor cyclability, and rate capability upon cycling compared with **CoTDC** (see Figure S27). To understand the enhanced redox kinetics of **CoTDC**, a galvanostatic intermittent titration technique (GITT) was employed to reveal the overpotential (η) differences (Figure 8a). The initial η value of $\mathbf{Li_2TDC}$ was approximately 95 mV owing to the kinetically favorable carboxylate-to-enolate reduction.[22] In contrast, the **CoTDC** electrode at the early lithiation (~15% SOC) exhibited a larger η value linked to the nucleation of metallic clusters and the corresponding rearrangement of local coordination structures. After the formation of $\mathbf{Co(0)}$ phase, however, the η value of **CoTDC** abruptly diminished to 94 mV, attributed to the corresponding carboxylate-to-enolate conversion (i.e., $\mathbf{Co(0)} + \mathbf{Li_2TDC} + 2Li \rightarrow \mathbf{Co(0)} + \mathbf{Li_4TDC}$). Then, the η values of both materials increased, where vinyl group reduction started. Notably, **CoTDC** exhibited a smaller η value than $\mathbf{Li_2TDC}$; the measured values of **CoTDC** were 162 and 159 mV at 50% SOC, whereas those of $\mathbf{Li_2TDC}$ were 235 and 211 mV (see the Figure 8a inset). To determine the dominant parameter affecting the reduced η values, charge-transfer resistance was evaluated from the semicircle of electrochemical impedance spectroscopy (see also Figures S28 and S29 in the Supporting Information). The Arrhenius plots for charge transfer were obtained by preparing symmetric cells at 50% SOC, while changing the temperature from 253 to 283 K (see Figure 8b). Yet, slight differences in the activation energies were found for **CoTDC** (65.0 kJ mol^{-1}) and $\mathbf{Li_2TDC}$ (68.2 kJ mol^{-1}).

We speculated that the enhanced electrochemical performance of **CoTDC** might be attributed to the enhanced electrical conduction path from in situ generated metallic $\mathbf{Co(0)}$ nanoparticles (eqs 1−2a).[56−58] To verify our hypothesis, pristine **CoTDC** was treated with reactive lithium metal assisted by a vortex mixer (see the Supporting Information, section I-1). This chemically lithiated sample showed XANES patterns similar to those of the electrochemically lithiated sample (Figure 8c). No lithium metal peak was detected in the ex situ XRD pattern afterward (Figure S30), indicating its reaction with **CoTDC**. The electrical conductivity of the chemically lithiated sample, $\mathbf{Co(0)}/\mathbf{Li_2TDC}$, was 2.48×10^{-6} S cm^{-1} comparable to the physical mixture of $\mathbf{Li_2TDC}$ and cobalt nanoparticles (Figure 8d), which suggests an electrical conduction network from the reduced metal domains.[5−9] Improved electrical conductivity in the presence of interconnected metallic cobalt nanoparticles may underlie the improved electrochemical performance (see also Figure 6b).[59,60]

4. CONCLUSIONS

In summary, we have successfully demonstrated that the metal-dependent solid-state redox reversibility of complex systems is governed by spatial proximity and binding affinity between 3d-metal and organic ligand matrix. Metallic cobalt nanoparticles in the size range of ~2−3 nm, well dispersed in the matrix, exhibit facile coordination with organic ligands. They can also offer electrical conduction paths that allow successive multielectron transfer to π-conjugated redox molecules. In stark contrast, the compositionally inhomogeneous copper clusters induce limited reconversion owing to an interfacial penalty. Comprehensive screening of coordination complexes aided by synthetic chemistry and electrochemical investigations leads to the high-capacity molecular complex, cobalt-2,5-thiophenedicarboxylate. We anticipate that this study has implications in the field of organic-based rechargeable batteries by elucidating the metal-dependent solid-state multistage redox behaviors.

■ ASSOCIATED CONTENT

Supporting Information

The Supporting Information is available free of charge on the ACS Publications website at DOI: 10.1021/acsami.8b04678.

Complete experimental procedures, reaction schemes, electrochemical performance, product characterizations, and DFT calculations (PDF)

■ AUTHOR INFORMATION

Corresponding Authors

*E-mail: hyunwooklee@unist.ac.kr (H.-W.L.).
*E-mail: ktlee@snu.ac.kr (K.T.L.).
*E-mail: syhong@unist.ac.kr (S.Y.H.).

ORCID

Jongnam Park: 0000-0002-0954-0172
Byeong-Kwan An: 0000-0003-1128-7505
Hyun-Wook Lee: 0000-0001-9074-1619
Kyu Tae Lee: 0000-0003-2769-3372
Sung You Hong: 0000-0002-5785-4475

Notes

The authors declare no competing financial interest.

■ ACKNOWLEDGMENTS

This work was supported by the National Research Foundation of Korea grant (NRF-2016R1A2B4015497). M.S.O. and N.P. acknowledge the support from BRL (NRF-2017R1A4A101532). The authors are grateful to Prof. Ja Hun Kwak for his valuable discussion.

■ REFERENCES

(1) Goodenough, J. B.; Park, K.-S. The Li-Ion Rechargeable Battery: A Perspective. *J. Am. Chem. Soc.* **2013**, *135*, 1167−1176.
(2) Su, X.; Wu, Q.; Li, J.; Xiao, X.; Lott, A.; Lu, W.; Sheldon, B. W.; Wu, J. Silicon-Based Nanomaterials for Lithium-Ion Batteries: A Review. *Adv. Energy Mater.* **2014**, *4*, 1300882.
(3) Park, C.-M.; Kim, J.-H.; Kim, H.; Sohn, H.-J. Li-Alloy Based Anode Materials for Li Secondary Batteries. *Chem. Soc. Rev.* **2010**, *39*, 3115−3141.
(4) Park, A.-R.; Park, C.-M. Cubic Crystal-Structured SnTe for Superior Li- and Na-Ion Battery Anodes. *ACS Nano* **2017**, *11*, 6074−6084.
(5) Kim, H.; Choi, W. I.; Jang, Y.; Balasubramanian, M.; Lee, W.; Park, G. O.; Park, S. B.; Yoo, J.; Hong, J. S.; Choi, Y.-S.; Lee, H. S.; Bae, I. T.;

DOI: 10.1021/acsami.8b04678
ACS Appl. Mater. Interfaces XXXX, XXX, XXX−XXX

Kim, J. M.; Yoon, W.-S. Exceptional Lithium Storage in a $Co(OH)_2$ Anode: Hydride Formation. *ACS Nano* **2018**, *12*, 2909−2921.
(6) Chun, J.; Jo, C.; Sahgong, S.; Kim, M. G.; Lim, E.; Kim, D. H.; Hwang, J.; Kang, E.; Ryu, K. A.; Jung, Y. S.; Kim, Y.; Lee, J. Ammonium Fluoride Mediated Synthesis of Anhydrous Metal Fluoride−Mesoporous Carbon Nanocomposites for High-Performance Lithium Ion Battery Cathodes. *ACS Appl. Mater. Interfaces* **2016**, *8*, 35180−35190.
(7) Croguennec, L.; Palacin, M. R. Recent Achievements on Inorganic Electrode Materials for Lithium-Ion Batteries. *J. Am. Chem. Soc.* **2015**, *137*, 3140−3156.
(8) Cabana, J.; Monconduit, L.; Larcher, D.; Palacín, M. R. Beyond Intercalation-Based Li-Ion Batteries: The State of the Art and Challenges of Electrode Materials Reacting through Conversion Reactions. *Adv. Mater.* **2010**, *22*, E170−E192.
(9) Poizot, P.; Laruelle, S.; Grugeon, S.; Dupont, L.; Tarascon, J.-M. Nano-Sized Transition-Metal Oxides as Negative-Electrode Materials for Lithium-Ion Batteries. *Nature* **2000**, *407*, 496−499.
(10) Larcher, D.; Tarascon, J.-M. Towards Greener and More Sustainable Batteries for Electrical Energy Storage. *Nat. Chem.* **2015**, *7*, 19−29.
(11) Schon, T. B.; McAllister, B. T.; Li, P.-F.; Seferos, D. S. The Rise of Organic Electrode Materials for Energy Storage. *Chem. Soc. Rev.* **2016**, *45*, 6345−6404.
(12) Lee, H. H.; Park, Y.; Kim, S. H.; Yeon, S.-H.; Kwak, S. K.; Lee, K. T.; Hong, S. Y. Mechanistic Studies of Transition Metal-Terephthalate Coordination Complexes upon Electrochemical Lithiation and Delithiation. *Adv. Funct. Mater.* **2015**, *25*, 4859−4866.
(13) Hong, S. Y.; Kim, Y.; Park, Y.; Choi, A.; Choi, N.-S.; Lee, K. T. Charge Carriers in Rechargeable Batteries: Na Ions vs. Li Ions. *Energy Environ. Sci.* **2013**, *6*, 2067−2081.
(14) Liang, Y.; Tao, Z.; Chen, J. Organic Electrode Materials for Rechargeable Lithium Batteries. *Adv. Energy Mater.* **2012**, *2*, 742−769.
(15) Poizot, P.; Dolhem, F. Clean Energy New Deal for a Sustainable World: from Non-CO_2 Generating Energy Sources to Greener Electrochemical Storage Devices. *Energy Environ. Sci.* **2011**, *4*, 2003−2019.
(16) Lee, M.; Hong, J.; Kim, H.; Lim, H.-D.; Cho, S. B.; Kang, K.; Park, C. B. Organic Nanohybrids for Fast and Sustainable Energy Storage. *Adv. Mater.* **2014**, *26*, 2558−2565.
(17) Kwon, M.-S.; Choi, A.; Park, Y.; Cheon, J. Y.; Kang, H.; Jo, Y. N.; Kim, Y.-J.; Hong, S. Y.; Joo, S. H.; Yang, C.; Lee, K. T. Synthesis of Ordered Mesoporous Phenanthrenequinone-Carbon via π-π Interaction-Dependent Vapor Pressure for Rechargeable Batteries. *Sci. Rep.* **2014**, *4*, 7404.
(18) Song, Z.; Qian, Y.; Gordin, M. L.; Tang, D.; Xu, T.; Otani, M.; Zhan, H.; Zhou, H.; Wang, D. Polyanthraquinone as a Reliable Organic Electrode for Stable and Fast Lithium Storage. *Angew. Chem., Int. Ed.* **2015**, *54*, 13947−13951.
(19) Nokami, T.; Matsuo, T.; Inatomi, Y.; Hojo, N.; Tsukagoshi, T.; Yoshizawa, H.; Shimizu, A.; Kuramoto, H.; Komae, K.; Tsuyama, H.; Yoshida, J.-i. Polymer-Bound Pyrene-4,5,9,10-tetraone for Fast-Charge and -Discharge Lithium-Ion Batteries with High Capacity. *J. Am. Chem. Soc.* **2012**, *134*, 19694−19700.
(20) Kim, D. J.; Hermann, K. R.; Prokofjevs, A.; Otley, M. T.; Pezzato, C.; Owczarek, M.; Stoddart, J. F. Redox-Active Macrocycles for Organic Rechargeable Batteries. *J. Am. Chem. Soc.* **2017**, *139*, 6635−6643.
(21) Nalluri, S. K. M.; Liu, Z.; Wu, Y.; Hermann, K. R.; Samanta, A.; Kim, D. J.; Krzyaniak, M. D.; Wasielewski, M. R.; Stoddart, J. F. Chiral Redox-Active Isosceles Triangles. *J. Am. Chem. Soc.* **2016**, *138*, 5968−5977.
(22) Armand, M.; Grugeon, S.; Vezin, H.; Laruelle, S.; Ribière, P.; Poizot, P.; Tarascon, J.-M. Conjugated Dicarboxylate Anodes for Li-Ion Batteries. *Nat. Mater.* **2009**, *8*, 120−125.
(23) Zhang, Z.; Yoshikawa, H.; Awaga, K. Monitoring the Solid-State Electrochemistry of Cu(2,7-AQDC) (AQDC = Anthraquinone Dicarboxylate) in a Lithium Battery: Coexistence of Metal and Ligand Redox Activities in a Metal−Organic Framework. *J. Am. Chem. Soc.* **2014**, *136*, 16112−16115.
(24) Li, G.; Yang, H.; Li, F.; Cheng, F.; Shi, W.; Chen, J.; Cheng, P. A Coordination Chemistry Approach for Lithium-Ion Batteries: The Coexistence of Metal and Ligand Redox Activities in a One-Dimensional Metal−Organic Material. *Inorg. Chem.* **2016**, *55*, 4935−4940.
(25) Fei, H.; Feng, W.; Xu, T. Zinc Naphthalenedicarboxylate Coordination Complex: A Promising Anode Material for Lithium and Sodium-Ion Batteries with Good Cycling Stability. *J. Colloid Interface Sci.* **2017**, *488*, 277−281.
(26) Xie, J.; Gu, P.; Zhang, Q. Nanostructured Conjugated Polymers: Toward High-Performance Organic Electrodes for Rechargeable Batteries. *ACS Energy Lett.* **2017**, *2*, 1985−1996.
(27) Zhao, Q.; Zhu, Z.; Chen, J. Molecular Engineering with Organic Carbonyl Electrode Materials for Advanced Stationary and Redox Flow Rechargeable Batteries. *Adv. Mater.* **2017**, *29*, 1607007.
(28) Lee, H. H.; Nam, D.; Kim, C.-K.; Kim, K.; Lee, Y.; Ahn, Y. J.; Lee, J. B.; Kwak, J. H.; Choe, W.; Choi, N.-S.; Hong, S. Y. Molecular Engineered Safer Organic Battery through the Incorporation of Flame Retarding Organophosphonate Moiety. *ACS Appl. Mater. Interfaces* **2018**, *10*, 10096−10101.
(29) He, S.; Li, Z.; Ma, L.; Wang, J.; Yang, S. Graphene Oxide-Templated Growth of MOFs with Enhanced Lithium-Storage Properties. *New J. Chem.* **2017**, *41*, 14209−14216.
(30) Li, C.; Hu, X.; Lou, X.; Chen, Q.; Hu, B. Bimetallic Coordination Polymer as A Promising Anode Material for Lithium-Ion Batteries. *Chem. Commun.* **2016**, *52*, 2035−2038.
(31) Shen, L.; Song, H.; Wang, C. Metal-Organic Frameworks Triggered High-Efficiency Li storage in Fe-Based Polyhedral Nanorods for Lithium-ion Batteries. *Electrochim. Acta* **2017**, *235*, 595−603.
(32) Song, H.; Shen, L.; Wang, J.; Wang, C. Reversible Lithiation−Delithiation Chemistry in Cobalt Based Metal Organic Framework Nanowire Electrode Engineering for Advanced Lithium-Ion Batteries. *J. Mater. Chem. A* **2016**, *4*, 15411−15419.
(33) Férey, G.; Millange, F.; Morcrette, M.; Serre, C.; Doublet, M.-L.; Grenèche, M.-M.; Tarascon, J.-M. Mixed-Valence Li/Fe-Based Metal−Organic Frameworks with Both Reversible Redox and Sorption Properties. *Angew. Chem., Int. Ed.* **2007**, *46*, 3259−3263.
(34) Wang, L.; Zhao, M.; Qiu, J.; Gao, P.; Xue, J.; Li, J. Metal Organic Framework-Derived Cobalt Dicarboxylate as a High-Capacity Anode Material for Lithium-ion Batteries. *Energy Technol.* **2017**, *5*, 637−642.
(35) Wang, F.; Kim, S.-W.; Seo, D.-H.; Kang, K.; Wang, L.; Su, D.; Vajo, J. J.; Wang, J.; Graetz, J. Ternary Metal Fluorides as High-Energy Cathodes with Low Cycling Hysteresis. *Nat. Commun.* **2015**, *6*, 6668.
(36) Park, Y.; Shin, D.-S.; Woo, S. H.; Choi, N. S.; Shin, K. H.; Oh, S. M.; Lee, K. T.; Hong, S. Y. Sodium Terephthalate as an Organic Anode Material for Sodium Ion Batteries. *Adv. Mater.* **2012**, *24*, 3562−3567.
(37) Wang, L.; Mou, C.; Sun, Y.; Liu, W.; Deng, Q.; Li, J. Structure-Property of Metal Organic Frameworks Calcium Terephthalates Anodes for Lithium-ion Batteries. *Electrochim. Acta* **2015**, *173*, 235−241.
(38) Nisula, M.; Karppinen, M. Atomic/Molecular Layer Deposition of Lithium Terephthalate Thin Films as High Rate Capability Li-Ion Battery Anodes. *Nano Lett.* **2016**, *16*, 1276−1281.
(39) Renault, S.; Oltean, V. A.; Araujo, C. M.; Grigoriev, A.; Edström, K.; Brandell, D. Superlithiation of Organic Electrode Materials: The Case of Dilithium Benzenedipropiolate. *Chem. Mater.* **2016**, *28*, 1920−1926.
(40) Lee, H. H.; Park, Y.; Shin, K.-H.; Lee, K. T.; Hong, S. Y. Abnormal Excess Capacity of Conjugated Dicarboxylates in Lithium-Ion Batteries. *ACS Appl. Mater. Interfaces* **2014**, *6*, 19118−19126.
(41) Han, X.; Qing, G.; Sun, J.; Sun, T. How Many Lithium Ions Can Be Inserted onto Fused C_6 Aromatic Ring Systems? *Angew. Chem., Int. Ed.* **2012**, *51*, 5147−5151.
(42) Rui, K.; Wen, Z.; Lu, Y.; Jin, J.; Shen, C. One-Step Solvothermal Synthesis of Nanostructured Manganese Fluoride as an Anode for Rechargeable Lithium-Ion Batteries and Insights into the Conversion Mechanism. *Adv. Energy Mater.* **2015**, *5*, 1401716.

DOI: 10.1021/acsami.8b04678
ACS Appl. Mater. Interfaces XXXX, XXX, XXX−XXX

(43) Luo, L.; Wu, J.; Xu, J.; Dravid, V. P. Atomic Resolution Study of Reversible Conversion Reaction in Metal Oxide Electrodes for Lithium-Ion Battery. *ACS Nano* **2014**, *8*, 11560−11566.
(44) Khatib, R.; Dalverny, A.-L.; Saubanère, M.; Gaberscek, M.; Doublet, M.-L. Origin of the Voltage Hysteresis in the CoP Conversion Material for Li-Ion Batteries. *J. Phys. Chem. C* **2013**, *117*, 837−849.
(45) Hannay, C.; Hubin-Franskin, M.-J.; Grandjean, F.; Briois, V.; Polian, A.; Trofimenko, S.; Long, G. J. X-ray Absorption Spectroscopic Study of the Temperature and Pressure Dependence of the Electronic Spin States in Several Iron(II) and Cobalt(II) Tris(pyrazolyl)borate Complexes. *Inorg. Chem.* **1997**, *36*, 5580−5588.
(46) Chadwick, A. V.; Savin, S. L. P.; Alcántara, R.; Lisbona, D. F.; Lavela, P.; Ortiz, G. F.; Tirado, J. L. X-ray Absorption Spectroscopic Study of $LiCoO_2$ as the Negative Electrode of Lithium-Ion Batteries. *ChemPhysChem* **2006**, *7*, 1086−1091.
(47) Aragón, M. J.; León, B.; Vicente, C. P.; Tirado, J. L.; Berko, A.; Beh, S.-Y. Cobalt Oxalate Nanoribbons as Negative-Electrode Material for Lithium-Ion Batteries. *Chem. Mater.* **2009**, *21*, 1834−1840.
(48) Herrero, E.; Li, J.; Abruña, H. D. Electrochemical, in-situ Surface EXAFS and CTR studies of Co monolayers irreversibly adsorbed onto Pt(111). *Electrochim. Acta* **1996**, *44*, 2385−2396.
(49) Wright, P. A.; Natarajan, S.; Thomas, J. M.; Gai-Boyes, P. L. Mixed-Metal Amorphous and Spinel Phase Oxidation Catalysts: Characterization by X-ray Diffraction, X-ray Absorption, Electron Microscopy, and Catalytic Studies of Systems Containing Copper, Cobalt, and Manganese. *Chem. Mater.* **1992**, *4*, 1053−1065.
(50) Inada, Y.; Sugimoto, K.; Ozutsumi, K.; Funahashi, S. Solvation Structures of Manganese(II), Iron(II), Cobalt(II), Nickel(II), Copper(II), Zinc(II), Cadmium(II), and Indium(III) Ions in 1,1,3,3-Tetramethylurea as Studied by EXAFS and Electronic Spectroscopy. Variation of Coordination Number. *Inorg. Chem.* **1994**, *33*, 1875−1880.
(51) Wang, F.; Robert, R.; Chernova, N. A.; Pereira, N.; Omenya, F.; Badway, F.; Hua, X.; Ruotolo, M.; Zhang, R.; Wu, L.; Volkov, V.; Su, D.; Key, B.; Whittingham, M. S.; Grey, C. P.; Amatucci, G. G.; Zhu, Y.; Graetz, J. Conversion Reaction Mechanisms in Lithium Ion Batteries: Study of the Binary Metal Fluoride Electrodes. *J. Am. Chem. Soc.* **2011**, *133*, 18828−18836.
(52) Pelliccione, C. J.; Ding, Y.; Timofeeva, E. V.; Segre, C. U. In Situ XAFS Study of the Capacity Fading Mechanisms in ZnO Anodes for Lithium-Ion Batteries. *J. Electrochem. Soc.* **2015**, *162*, A1935−A1939.
(53) Fu, Z.-W.; Huang, F.; Zhang, Y.; Chu, Y.; Qin, Q.-Z. The Electrochemical Reaction of Zinc Oxide Thin Films with Lithium. *J. Electrochem. Soc.* **2003**, *150*, A714−A720.
(54) Demessence, A.; Rogez, G.; Welter, R.; Rabu, P. Structure and Magnetic Properties of a New Cobalt(II) Thiophenedicarboxylate Coordination Polymer Showing Unprecedented Coordination. *Inorg. Chem.* **2007**, *46*, 3423−3425.
(55) Ning, Y.; Lou, X.; Li, C.; Hu, X.; Hu, B. Ultrathin Cobalt-Based Metal−Organic Framework Nanosheets with Both Metal and Ligand Redox Activities for Superior Lithium Storage. *Chem.—Eur. J.* **2017**, *23*, 15984−15990.
(56) Taberna, P. L.; Mitra, S.; Poizot, P.; Simon, P.; Tarascon, J.-M. High Rate Capabilities Fe_3O_4-Based Cu Nano-Architectured Electrodes for Lithium-Ion Battery Applications. *Nat. Mater.* **2006**, *5*, 567−573.
(57) Liu, Y.; He, X.; Hanlon, D.; Harvey, A.; Khan, U.; Li, Y.; Coleman, J. N. Electrical, Mechanical, and Capacity Percolation Leads to High-Performance MoS_2/Nanotube Composite Lithium Ion Battery Electrodes. *ACS Nano* **2016**, *10*, 5980−5990.
(58) Zhang, B.; Yu, Y.; Huang, Z.-D.; He, Y.-b.; Kim, J.-K. Percolation Threshold of Graphene Nanosheets as Conductive Additives in $Li_4Ti_5O_{12}$ Anodes of Li-Ion Batteries. *Nanoscale* **2013**, *5*, 2100−2106.
(59) Li, Y.; Tan, B.; Wu, Y. Mesoporous Co_3O_4 Nanowire Arrays for Lithium Ion Batteries with High Capacity and Rate Capability. *Nano Lett.* **2008**, *8*, 265−270.
(60) Sauvage, F.; Tarascon, J.-M.; Baudrin, E. In Situ Measurements of Li Ion Battery Electrode Material Conductivity: Application to Li_xCoO_2 and Conversion Reactions. *J. Phys. Chem. C* **2007**, *111*, 9624−9630.

DOI: 10.1021/acsami.8b04678
ACS Appl. Mater. Interfaces XXXX, XXX, XXX−XXX